RSC Advances

ROYAL SOCIETY OF CHEMISTRY

www.rsc.org/advances

Graphical abstract

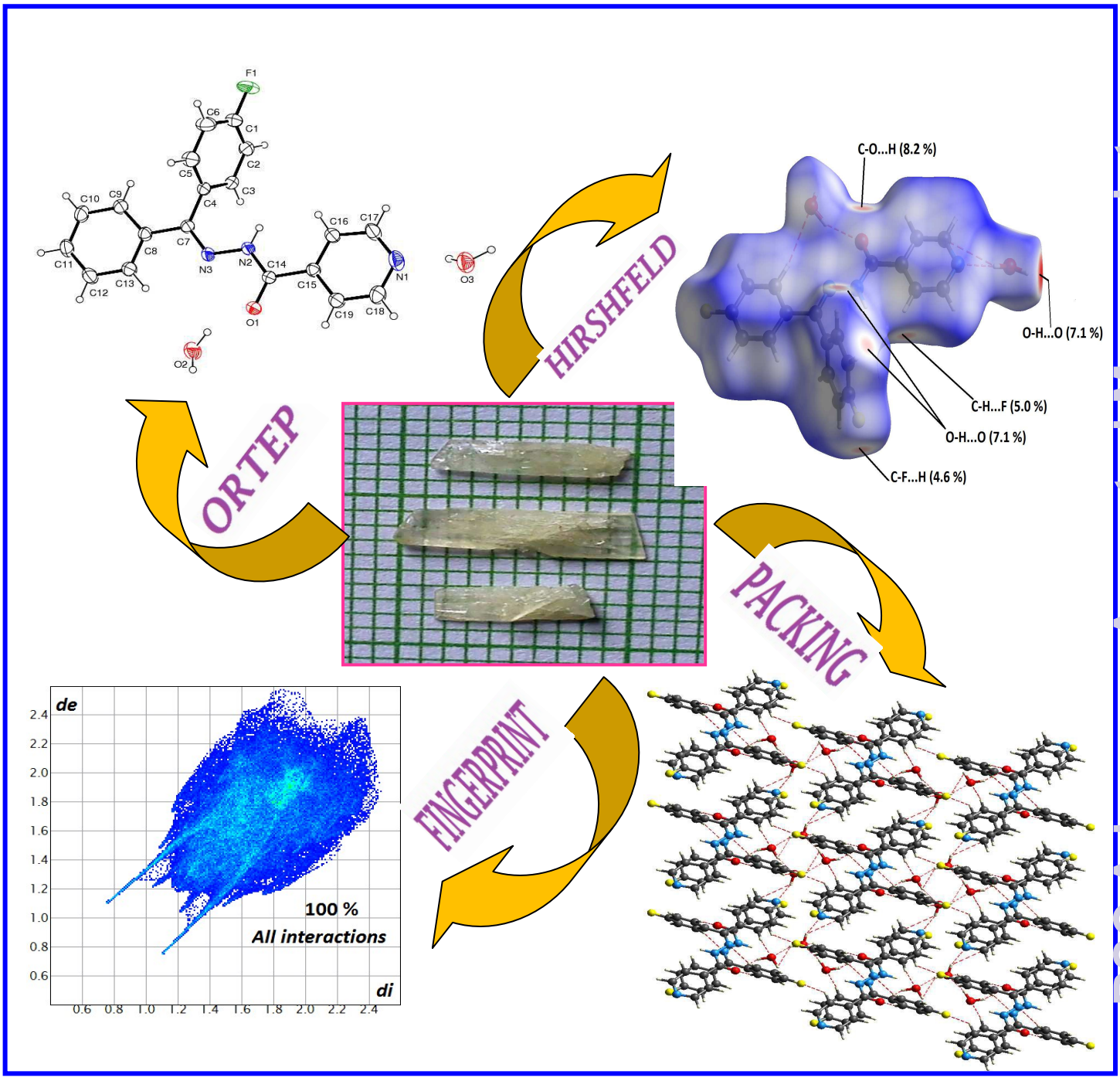

Cite this: DOI: 10.1039/c0xx00000x

www.rsc.org/xxxxxx

FULL PAPER

Synthesis, growth, spectral studies, first-order molecular hyperpolarizability and Hirshfeld surface analysis of isonicotinohydrazide single crystals

V. Meenatchi and SP. Meenakshisundaram*

* *Department of Chemistry, Annamalai University, Annamalai Nagar – 608002. E-mail aumats2009@gmail.com, Tel. +91 9943114904.*

Received (in XXX, XXX) Xth XXXXXXXXX 20XX, Accepted Xth XXXXXXXXX 20XX

DOI: 10.1039/b000000x

Single crystals of (E)-N'-((4-fluorophenyl)(phenyl)methylene)isonicotinohydrazide dihydrate were grown by the slow evaporation solution growth technique. The structure is elucidated by single crystal X-ray diffraction analysis and the crystal belongs to the triclinic system with space group $P\bar{1}$. The crystallinity of the material was confirmed by powder X–ray diffraction which well coincides with simulated pattern with varied intensities pattern. The band gap energy is estimated by the application of Kubelka–Munk algorithm. Theoretical calculations were performed using density functional theory (DFT), to derive the optimized geometry, dipole moment, HOMO-LUMO energies and first–order molecular hyperpolarizality, β (~ 84 times of urea). The energy and oscillator strength calculated by TD-DFT results complement with the experimental findings. The atomic charge distributions of the various atoms are obtained by Mulliken charge population analysis. The molecular stability and bond strength were investigated by applying the natural bond orbital analysis. Investigation of the intermolecular interactions and crystal packing *via* Hirshfeld surface analysis, based on single-crystal XRD, reveals that the close contacts are associated with molecular interactions. Fingerprint plots of Hirshfeld surfaces were used to locate and analyze the percentage of hydrogen-bonding interactions. The grown crystals were further characterized by FT-IR, FT-Raman and TG/DTA.

1. Introduction

Organic single crystals possess unique optoelectronic properties because the molecules have delocalized electrons exhibiting various photoresponses such as photoconductive, photovoltaic, photocatalytic behavior and so on. Isoniazid, the hydrazide of isonicotinic acid is recognized as an effective antituberculous agent and employed in the treatment and prevention of TB disease, not only as a single drug but also combined with others. The hydrazone group plays an important role for the antimicrobial activity and possesses interesting antibacterial, antifungal[1-3], anti–tubercular activities[4-9]. In spite of the toxicity on repeated dosing, isonicotinylhydrazone (INH) is still considered to be a first line drug for chemotherapy of tuberculosis[10]. Aromatic hydrazone molecules dispersed in a binder polymer are used as the main constituent of electrophotographic devices due to their excellent hole-transporting properties and relatively simple synthesis [11-14]. Recently, we have reported synthesis, growth characterization and theoretical studies of 4-benzoylpyridine isonicotinyl hydrazone monohydrate[15], benzophenone-2-furoyl hydrazone[16] and (E)-N'-(Diphenylmethylene)isonicotinohydrazide dihydrate[17]. The growth, structure and characterization of (E)-N'-((4-fluorophenyl)(phenyl)methylene)isonicotinohydrazide dihydrate

(FPMI) have not been reported so far to the best of our knowledge. In the present study, we report synthesis, growth, structure, optical, dipole moment, first-order molecular hyperpolarizability, Hirshfeld surface and finger print analysis of organic crystal (E)-N'-((4-fluorophenyl) (phenyl)methylene)isonicotinohydrazide dihydrate. Experimental observations are mostly supported by theoretical studies.

2. Experimental

2.1 Synthesis and crystal growth

(E)-N'-((4-fluorophenyl)(phenyl)methylene)iso nicotinohydrazide dihydrate (FPMI) was synthesized by mixing stoichiometric amounts of *p*-fluorobenzophenone (Sigma Aldrich) and isoniazid (Sigma Aldrich) in the molar ratio of 1:1 (**Scheme 1**). The reactants were dissolved in ethanolic medium with catalytic amount of concentrated sulphuric acid and refluxed for 3–5 h to form aryl acid hydrazone. The product formation was identified by thin layer chromatography. The reaction mixture was then poured in ice cold water and the precipitate obtained was filtered and dried. Purity of the compound was improved by successive recrystallization process using ethanol as a solvent.

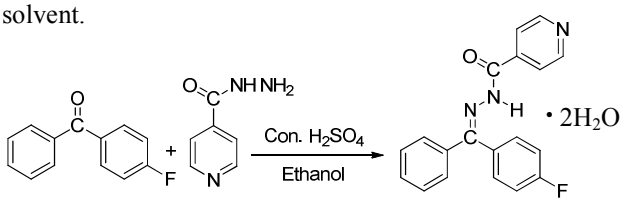

Scheme 1

2.2. Crystal growth

FPMI single crystals were grown by the slow evaporation solution growth technique at room temperature. A saturated solution of FPMI in ethanol was prepared and the solution was stirred for 2–3 h at room temperature to obtain a homogenous solution. A beaker containing the solution was tightly covered with a thin polythene sheet to control the evaporation rate of the solvent and kept undisturbed in a dust free environment. Numerous plates like crystals were formed at the bottom of the container due to spontaneous nucleation. Macroscopic defect–free crystals were harvested after a period of 9 to 11 d and the photographs of as–grown crystals are shown in **Fig. 1.**

2.3. Computational details

Computational studies were done using the *GAUSSIAN09W*[18] software package without any constraints on the geometry using the density functional theory (DFT) and the molecules has visualized *GAUSSVIEW* 5.0 program[19]. Hirshfeld surfaces and fingerprint plots were generated from the crystal data using the DFT method with 6-31G(d,p) as basis set[20].

3. Results and discussion

3.1. FT-IR and FT-Raman

The characteristic vibrational bands observed in the FT–IR (experimental and theoretical) and FT–Raman spectra are shown in **Figs. S1 and S2 (See ESI).** The molecular structure of FPMI consists of 44 atoms, 186 electrons and hence this molecule has 126 normal modes of vibration. The molecular conformation yielded by geometry optimization exhibits no special symmetries and hence the molecule belongs to the C_1 point group. The C=O stretching vibration is observed at 1672 cm^{-1} (theoretically 1665 cm^{-1}). The C=N stretching vibration appeared as sharp intensity band around 1600 cm^{-1} (theoretically 1607 cm^{-1}). The absorption band around 1128 cm^{-1} (theoretically 1127 cm^{-1}) corresponds to O=C-N stretching vibrations. The peak at 770 cm^{-1} (theoretically 792 cm^{-1}) is aromatic C-H out of plane bending vibrations respectively. The peak at 1034 cm^{-1} (theoretically 1028 cm^{-1}) corresponds to C-F stretching vibration. The observed FT–IR and FT–Raman vibrational bands of FPMI are listed along with literature[15-17, 21-24] data for some hydrazones as a comparative measure in **Table 1.**

3.2. Optical studies

The Kubelka–Munk theory[25] provides a correlation between reflectance and concentration. The concentration of an absorbing species can be determined using the Kubelka–Munk formula,

$$F(R) = (1 - R)^2 / 2R = \alpha/s = Ac/s$$

where *F(R)* is Kubelka – Munk fuction, R is the reflectance of the crystal, α is absorption coefficient and s is scattering coefficient, A is the absorbance and c is concentration of the absorbing species. The direct and indirect band gap energies obtained from the intercept of the resulting straight lines with the energy axis at $[F(R)hv]^2 = 0$ and $[F(R)hv]^{1/2} = 0$ are 3.21 eV (direct) and 2.96 eV (indirect) respectively as shown by Tauc plots in **Fig. S3.**

The optical absorbance spectrum of FPMI was recorded in the spectral range of 200 to 600 nm as shown in **Fig. 2a.** It reveals that the absorbance is minimum in the visible region with wavelength cut–off at ~ 304 nm. UV-vis spectral data of FPMI are calculated by TD-DFT/ ZINDO/ CIS methods and the absorption peak, excitation energy and oscillator strength values are summarized in **Table 2.** The theoretical spectra of FPMI are shown in **Fig. 2b-d.** It appears that the ZINDO method is more accurate. Since it closely resembles the experimental value.

3.3. Thermal analysis

In order to test the thermal stability of FPMI the thermogravimetric analysis (TG) and differential thermal analysis (DTA) have been carried out simultaneously. The TG/DTA response curve is shown in **Fig. S4.** From the figure it is observed that TG curve loses 10 % of mass due the removal of water molecule (experimentally observed loss: 3.6 %; theoretically expected: 3.5 %). In DTA curve the endothermic peak observed at 115 °C is attributed to melting of the FPMI crystal. In the TG curve the major weight loss is from 300 to 400 °C. It is clearly revealed that mass of the samples remains unchanged till a temperature of 300 °C and loses its weight almost completely at around 400 °C. This variation in weight loss after 300 °C indicates the decomposition of the sample and it is extends up to 400 °C. No exothermic or endothermic peak was observed below the melting point endotherm, indicating the absence of any isomorphic phase transition in the sample. The sharpness of the endothermic peak shows good degree of crystallinity of the as–grown material.

3.4. X-ray diffraction analysis

As–grown FPMI crystal was finely powdered and subjected to powder XRD analysis. The indexed powder XRD pattern of as–grown FPMI is shown in **Fig. 3** along with simulated one. The XRD profiles show that the sample is of single phase without a detectable impurity. The well defined Bragg peaks at specific 2θ angles show high crystallinity of the material. Most of the peak positions in powder and simulated X-ray diffraction patterns from single crystal XRD coincide but the relative intensities differ. Possibly this could be due to preferred orientations of the sample used for diffractogram measurement and the difference in mosaic spread of powder and single crystal patterns.

FPMI crystal belongs to the triclinic system with centrosymmetric space group $P\bar{1}$. The *ORTEP* and packing diagrams are shown as **Fig. 4** and the crystal data are given in **Table 3.**

In the title compound the fluorine atom is disordered over two positions with the site occupancy ratio of 63:37. The anisotropic displacement parameters of the disordered atom were restrained with effective standard deviation of 0.02 $Å^2$. The O1 atom and the hydrazinic N3 atom are *cis* with respect to C14-N2 bond. The structure of the compound reveals the quasi coplanarity of the whole molecular skeleton with localization of the double bonds in the central >C=N-N-C=O which has an E–configuration with respect to the double bond of the hydrazone bridge. A *trans* configuration is fixed around the N2-N3 single bond of length 1.3800 (16) Å. The central part of the molecule C7-N3-N2-C14-O1, adopts a completely extended conformation. The bond lengths C7-N3 (1.2891(18) Å) andC14-O1 (1.2182(16) Å) are typical of double bonds. In the crystal structure, molecules are linked through intermolecular C—H---O, C—H---F, O—H---O and O—H---N hydrogen bonds **(Fig. 4(c)).** The hydrogen bond symmetry is listed in **Table 4.**

The experimental and calculated data refer to bond length (exp) and bond length (cal), respectively. The

agreement between the theoretical and experimental results has been expressed by root mean square (RMSD) deviation using the following expression.

$$\mathrm{RMSD} = \sqrt{\frac{1}{n-1}\Sigma_i^n \left(\gamma_i^{cal} - \gamma_i^{exp}\right)^2}$$

where n is the number. The RMSD of the observed single crystal XRD bond length is found to be of 0.5160 % error. It is caused by neglecting anharmonicity and electron correlation.

3.5. First-order molecular hyperpolarizability

The calculated polarizability (α), first–order molecular hyperpolarizability *(β)* and dipole moment (μ) of the specimen are 37.10×10^{-24} esu, 23.458×10^{-30} esu (~84 times of urea) and 8.4513 D, respectively **(Table 5).** The maximum value of hyperpolarizability is due to the nonzero μ values. High *β* is associated with high charge transfer. The *β* values of some hydrazide derivatives are listed in **Table 6**. It is interesting to observe that the substitution of fluorine in the *para* position of benzophenone ring enhances the hyperpolarizability significantly i.e., ~16 times of unsubstituted hydrazide which is ~84 times of urea. But even this significant rise in *β* could not be translated at the macro level and negligible second harmonic generation efficiency is observed due to orientation effect resulting in a centrosymmetric structure. The optimized molecular structure of FPMI **(Fig. 4(b))** closely resembles the displacement ellipsoid diagram **(Fig. 4(a)).**

3.6. Molecular electrostatic potential

Molecular electrostatic potential (MEP) at a point in the space around a molecule gives an indication of the net electrostatic effect produced at that point by the total charge distribution (electron + proton + nucleus) of the atom or molecule and correlates with dipole moments, electronegativity, partial charges and chemical reactivity of the molecule. The different values of the electrostatic potential at the surface are represented by different colors: red represents regions of most negative electrostatic potential, blue represents regions of most positive electrostatic potential, and green represents regions of zero potential. The order of increase of potential is, red < orange < yellow < green < blue. The electrophiles tend to the negative and the nucleophiles tend to the region of positive MEP **(Fig. 5a).** In FPMI, the carbonyl group behaves as electrophilic region and it is denoted as red color. Likewise, the nucleophilic region was graphically shown as blue color. Molecular surfaces obtained by B3LYP level 6-31G(d,p) as the basis set are shown in **Fig. 5.**

3.7. Mulliken population analysis

In the application of quantum mechanical calculations to molecular systems, the calculation of effective atomic charge plays an important role. Mulliken atomic charges are calculated by determining the electron population of each atom as defined by the basis function. **Fig. 6a** and **Fig. 6b** show the Mulliken atomic charges of FPMI. From the atomic charge values the oxygen (O26, O37 and O40), nitrogen (N22, N23 and N34), fluorine (F44) and carbon (C1-C5, C12-C17, C28 and C29) in FPMI had a large negative charge and behaved as electron donors. The remaining atoms are acceptors exhibiting positive charge. The negative charges on nitrogen/oxygen/fluorine, which is a donor atom and net positive charge on hydrogen atom, which is an acceptor atom, suggest the presence of intermolecular hydrogen bonding interactions in FPMI. Hydrogen bonding interactions are clearly shown by the packing diagram of single crystal XRD data **(Fig. 5(c)).**

3.8. Natural bond orbital (NBO) analysis

The NBO analysis examines all possible interactions between filled (donor) Lewis-type NBOs and empty (acceptor) non-Lewis NBOs and estimating their energetic importance by second-order perturbation theory[26].The one-centre lone pairs and two-centre bonds from NBO analysis present an exact representation of chemical bonding for a stable molecular species, corresponding to a single Lewis structure. The non-Lewis set includes unoccupied valence nonbonding (LP*) and

extra-valence-shell Rydberg (RY*) orbitals as well as the valence antibonds (BD*) The deficiency of the Lewis type NBOs (bonds and lone pairs) in representing the density matrix can be quantified with the occupancy of these NBOs. The energy of the delocalization, ΔE_{ij} is calculated as

$$E^{(2)}=\Delta E_{ij} = q_i F(i,j)^2 /(\varepsilon_j - \varepsilon_i)$$

Where $E^{(2)}$is the energy of hyperconjugative interactions. qi is the occupancy of the donating (Lewis type) orbital, εi and εj are the energies of the donating and accepting orbitals, and F_{ij} is the off-diagonal element of the Fock matrix in the NBO basis[27]. NBO analysis has been performed on the FPMI molecule at the B3LYP/6-31G(d,p) level in order to explain the intra molecular hybridization and delocalization of electron density within the molecule. The intramolecular hyperconjugative interactions of σ(C10-N22) orbital to σ*(C12-C14) lead to strong stabilization energies of 0.65 kJ/mol. The most important interaction energy in this molecule is electron donating from LP (N23) to the antibonding acceptor π*(C25-O26) resulting less stabilization energy of 51.58 kJ/mol. The same σ (N23) with π*(C25-O26) leads to moderate stabilization energy of 27.84 KJ/mol. LP (N23) to the antibonding acceptor σ*(C25-O26) leads to strong stabilization energy of 1.12 kJ/mol. The maximum stabilization delocalization takes part in the σ–σ* transition. The $E^{(2)}$ values and types of the transition are shown in **Table 7.**

3.9. Hirshfeld surfaces analysis

The Hirshfeld surfaces of FPMI has been demonstrated in **Fig. 7,** showing surfaces that have been mapped over a d_{norm}, *shapeindex*, curvedness, d_e and d_i. The Hirshfeld surface [28-30] surrounding a molecule is defined by points where the contribution to the electron density from the molecule under contribution is equal to the contribution from all the other molecules. For each point on that isosurface two distances are determined: one is d_e representing the distance from the point to the nearest nucleus external to the surface, and the second is di representing the distance to the nearest nucleus internal to the surface. The normalized contact distance (*dnorm*) based on both *de* and *di*. The surfaces are shown as transparent to allow visualization of the molecule, around which they were calculated. Hydrogen bonding contacts are revealed by circular depressions (deep red) visible on the Hirshfeld surface, and the other visible spots are due to hydrogen bonding interactions. O…H (8.2%), H…O (7.1%), H…F (5.0%), F…H (4.6%) and F…F (2.1%) contacts **Fig. 7a** and O…H (8.2%), H…O (7.1%), H…F (5.0%), F…H (4.6%) and F…F (2.1%) **Fig. 7b.** The deep red colour spots in *de* **(Fig. 7c)** are strong interactions such as O…H (8.2%). The dominant interactions are H…O (7.1 %) and H…F (5.0 %) can be seen in *di* surface plots as the bright red area in **Fig. 7d.** Hirshfeld surfaces of individual molecule are given in **Fig. 7** for a better understanding of molecular interactions. The red spots on the surface indicate close contacts. The *shapeindex* indicate the shape of electron density surface around the molecular interactions. The small range of area and light color on the surface represents a weaker and longer contact other than hydrogen bonds. The *curvedness* surface indicates the electron density surface curves around the molecular interactions. Three dimendional images of crystal packing along a-axis, b-axis and c-axis are shown in **Figs. 8-10**. The deformation density the difference between the total electron density of a molecule and the electron density of "neutral spherical unperturbed atoms" superimposed at the same atomic positions of the molecule is calculated as 0.008 (maximum) and -0.008 a.u. (minimum) (a.u. is atomic units). A graphical view of deformation density is shown in **Fig. 11**.

3.10. Fingerprint analysis

The two-dimensional fingerprint plots[30] of FPMI exemplify the strong evidence for the intermolecular interactions pattern. In the fingerprint plot (**Fig. 12**), O…H (8.2 %) interactions are represented by a spike at the bottom of the plot whereas the H…O (7.1 %) interactions are represented by a spike in the top left region. Hydrogen bonding interactions H…H (40.4 %) are very high while compared to the other bonding interactions. Sharp curved

spike at the bottom left area indicates the H…F (5.0 %) and top left corner with curved spike indicates the F…H (4.6 %). The finger print at the bottom right area represents H…C (9.6 %) interactions and top right area represents C…H (7.2 %) interactions. The finger print at the bottom right area represents N…H (2.3 %) interactions and top right area represents H…N (1.8 %) interactions. Sharp curved spike at the centre area indicates the F…F (2.1%) interactions. The combination of *de* and *di* in the form of a two-dimensional fingerprint plot provides a summary of intermolecular contacts in the crystal. The numbers of interactions interms of percentage are represented in a pie chart **(Fig.13).**

4. Conclusions

Single crystals of (E)-N'-((4-fluorophenyl) (phenyl)methylene)isonicotinohydrazide dihydrate were successfully synthesized and grown by the slow evaporation solution growth method at room temperature. The grown crystals have been subjected to various characterization studies. The functional groups of the grown compound have been identified by FT-IR and FT-Raman analyses. The total molecular weight was confirmed by mass spectral analysis. The number of protons and carbons present in the compound were confirmed by NMR analysis. The crystallographic data indicate that the FPMI crystallizes in the triclinic system with centrosymmetric space group *P*1 while the precursor benzophenone belongs to the orthorhombic system with noncentrosymmetric space group $P2_12_12_1$.The minimum absorption in the visible region is observed from the UV-vis measurement. It is an important requirement for the materials having NLO properties. Optimized geometrical parameters are close to the experimental values. Molecular stability was successfully analysed using NBO second order Fock matrix analysis. Electron delocalization is confirmed by MEP, ESP, total density and alpha density maps. The intermolecular charge transfer is evidenced by Mulliken charge population analysis. High first-order molecular hyperpolarizability associated with high charge transfer clearly reveals the molecular level nonlinearity. The analysis of Hirshfeld surface derived fingerprint plots an effective method to identify different types of intermolecular interactions. Further work is in progress to design a noncentrosymmetric structure so that nonlinearity at the macrolevel can be achieved.

Supporting Information

CCDC 947423 contains the supplementary crystallographic data for this paper. These data can be obtained free of charge from The Cambridge Crystallographic Data Centre via www.ccdc.cam.ac.uk/data request/cif.

Supplementary information contains characterization techniques (methodology), FT-IR vibrational modes (experimental and theoretical), FT-Raman, band gap energy and thermal analyses.

Acknowledgement

The authors thank SAIF, IIT Madras, Chennai for providing single crystal XRD facility .The authors thank the Council of Scientific and Industrial Research (CSIR), New Delhi, for financial support through research grant No.03(1233)/12/EMR-II, and VM is grateful to CSIR project for the award of SRF (Extended).

References

1 C. Loncle, J.M. Brunel, N. Vidal. M. Dherbomez and Y. Letourneux, *Eur. J. Med. Chem.*, 2004, 39, 1067-1071.

2 S. Papakonstantinou-Garoufalias, N. Pouli, P. Markos and A. Chytyroglou-Ladas, *II Farmaco,* 2002, 57, 973-977.

3 P. Vicini, F. Zani, P. Cozzini and I. Doytchinova, *Eur. J. Med. Chem.,* 2002, 37,553-564.

4 B.K. Kaymakcroglu and S. Rollas, *II Farmaco,* 2002, 57, 595-599.

5 R. Maccari, R. Ottana and M.G. Vigorita, *Bioorg.Med. Chem. Lett.,* 2005,15, 2509-2513.

6 M.T. Cocco, C. Congiu, V. Onnis, M.C. Pusceddu, M.L. Schivo and A. Logu, *Eur. J. Med. Chem.*, 1999, 34, 1071-1076.

7 D.G. Rando, D.N. Sato, L. Siqueira, A. Malvezzi, C.Q.F. Leite, A.T. Amaral, E.I. Ferreira and L.C. Tavares, *Bioorg. Med. Chem.,* 2002, 10, 557-560.

8 J. Patole, D. Shingnapurkar, S. Padhye and C. Ratledge, *Bioorg. Med. Chem. Lett.,* 2006, 16, 1514-1517.

9 A. Maiti and S. Ghosh, *J. Inorg. Biochem.,* 1989, 36, 131-139.

10 D. Sriram, P. Yogeeswari and K. Madhu, *Bioorg. Med. Chem. Lett.,* 2005,15, 4502-4505.

11 N. Mori, US patent No. 5, 567, 557, 1996.

12 N. Tatsya, U. Minoru, Japan Patent No. 8, 101, 524, 1996.

13 Y. Suzuki, US Patent No. 5, 6656, 500 1997.

14 N. Jurban, Z. Tokarski and T.P. Smith, US Patent No. 6, 340, 548, 2002.

15 V. Meenatchi, K. Muthu, M. Rajasekar and SP. Meenakshisundaram, *Spectrochimica Acta Part A.,* 2014, 124, 423-428.

16 V. Meenatchi, K. Muthu, M. Rajasekar and SP. Meenakshisundaram, *Optik,* 2014, 125, 4196 – 4200.

17 V. Meenatchi, K. Muthu, M. Rajasekar, G. Bhagavannarayana and SP. Meenakshisundaram, *Optik,* 2014, 125, 4181 – 4185.

18 M. J. Frisch, G. W. Trucks et al., *Gaussian09, Revision C.01*, Gaussian, Inc., Wallingford CT, 2009.

19 R. Dennington, T. Keith and J. Millam, *GaussView, Version 5, Semichem Inc*., Shawnee Mission KS, 2009.

20 B. Schlegel, *J. Comp. Chem.,* 1982, 3, 214-218.

21 R.M. Silverstein, F.X. Webster, D.J. Kiemle, Spectroscopic identification of organic compounds, seventh edition, John Wiley & Sons, 2005.

22 S. Sylvestre and K. Pandiarajan, *Spectrochim. Acta Part A.,* 2011, 78,153 – 159.

23 N. Ramesh Babu, S. Subashchandrabose, M.Syed Ali Padusha, H.Saleem,V.Manivannan and Y. Erdogdu, *J. Mole. Struc.,* 2014,1072, 84 – 93.

24 A. Manimekalai, N. Saradhadevi and A. Thiruvalluvar, *Spectrochim. Acta Part A.,* 2010, 77, 687 – 695.

25 P. Kubelka and F. Munk, Zeitschrift fur technische Physik, 1931,12, 593-601.

26 E.D. Glendening, J.K. Badenhoop, A.D. Reed, J.E. Carpenter and F. Weinhold, NBO 3.1, *Theoretical Chemistry Institute*, University of Wisconsin, Madison, WI(1996).

27 J. J. Dannenberg, Chem. Rev. 1999, 99, 1225-1241.

28 F. L. Hirshfeld, *Theor. Chim. Acta*, 1977, 44, 129–138.

29 CrystalExplorer (Version 3.1), S.K. Wolff, D.J. Grimwood, J.J. McKinnon, M.J. Turner, D. Jayatilaka and M.A. Spackman, University of Western Australia, 2012.

30 M.A. Spackman and J.J. McKinnon, *Cryst.Eng.Comm.,* 2002, 4, 378-392

Table 1 Observed vibrational bands of FPMI (cm^{-1}).

Assignments of vibration	FPMI		BPIH [(a)]		BPFH[(b)]	DPMI[(c)]	PMBH[(d)]		MPNH[(e)]	MPINH[(f)]
	FT–IR	FT–Raman	FT–IR	FT–Raman	FT-IR	FT-IR	FT–IR	FT–Raman	FT–IR	FT–IR
C=O stretching	1672	1663	1672	1694	1687	1699	1697	1683	1637	1671
C=N stretching	1600	1601	1597	1599	1627	1639	1611	1627	1594	1647
C=C stretching	1507	1506	1507	1493	1513	1498	1582	1580	1548	1557
C-H stretching	3073	3072	3057	3061	3000 - 3100	3000 - 3100	3085, 3168	3100	3079	3026
N-H stretching	3452	--	3452	--	3351 and 3435	3427	3349	--	3444	3452
O=C-N stretching	1128	1130	1130	1133	1123	1118	--	--	--	--
C-F stretching	1034	1032	--	--	--	--	--	--	--	--

(a) ref [15], (b) ref [16], (c) ref [17], (d) ref [23], (e) ref [24] and (f) ref [24].

Table 2 Theoretical electronic absorption spectral values of FPMI

Method	**Wavelength (λ_{max}, nm)**	**Excitation energies (eV)**	**Oscillator strengths (f)**
ZINDO	304	3.0437	0.7465
TD-DFT	331	3.3198	0.5841
CIS	237	2.3740	0.904

Table 3 Crystal data and structure refinement for FPMI.

Empirical formula	**$C_{19}H_{18}FN_3O_3$**
Formula weight	355.36
Temperature	293(2) K
Wavelength	0.71073Å
Crystal system, space group	Triclinic, $P\bar{1}$
Unit cell dimensions	a = 8.6739(4) Å, α = 75.1390(10)° b = 9.7386(4) Å, β = 74.865(2)° c = 11.1516(5) Å, γ= 88.181(2)°
Volume	878.28(7) $Å^3$
Z, Calculated density	2, 1.344 Mg/m^3
Absorption coefficient	0.100 mm^{-1}
F(000)	372
Crystal size	0.35 x 0.30 x 0.30 mm^3
Theta range for data collection	2.17 to 25.00 °
Limiting indices	$-10 \le h \le 10$, $-11 \le k \le 11$, $-13 \le l \le 13$
Reflections collected/unique	15680 / 3108 [R(int) = 0.0257]
Completeness to theta = 22.20	99.9 %
Absorption correction	Semi-empirical from equivalents
Max. and min. transmission	0.9836 and 0.9536
Refinement method	Full-matrix least-squares on F^2
Data/restraints/parameters	3108 / 7 / 266
Goodness-of-fit on F^2	1.058
Final R indices [I > 2sigma(I)]	R1 = 0.0384, wR2 = 0.1055
R indices (all data)	R1 = 0.0470, wR2 = 0.1124
Extinction coefficient	0.012 (3)
Largest diff. peak and hole	0.179 and -0.131 e. $Å^{-3}$

Table 4 Hydrogen bonds geometry of FPMI (Å, °).

D-H---A	**d(D-H)**	**d(H---A)**	**D(D---A)**	**<(DHA)**
C(2)-H(2)...O(3)$^{\#1}$	0.93	2.55	3.413(2)	153.7
C(16)-H(16)...F(1)$^{\#2}$	0.93	2.38	3.173(2)	143.1
O(2)-H(2A)...O(3)$^{\#3}$	0.904(16)	1.921(16)	2.813(2)	169(2)
O(2)-H(2B)...O(1)	0.900(16)	2.005(19)	2.8521(17)	156(2)
O(3)-H(3A)...N(1)	0.902(16)	2.003(17)	2.8491(19)	156(2)
O(3)-H(3B)...O(2)$^{\#4}$	0.897(16)	1.933(17)	2.7841(18)	158(2)

Symmetry transformations used to generate equivalent atoms: #1 x,y+1,z ; #2 -x,-y+2,-z+3; #3 -x+1,-y+1,-z+2; #4 x,y-1,z+1.

Table 5 The calculated dipole momement (in D), β components (a.u), β_{tot} value (in esu), α components (a.u), α_{tot} value (in esu) and HOMO – LUMO (eV) characteristic for FPMI.

First-order molecular hyperpolarizability	
β_{xxx}	2514.006
β_{xxy}	21.951
β_{xyy}	162.925
β_{yyy}	127.131
β_{xxz}	-52.112
β_{xyz}	25.779
β_{yyz}	-31.628
β_{xzz}	33.914
β_{yxx}	-13.582
β_{zzz}	8.221
β_{tot} (x10^{-30})	23.458
Polarizability	
α_{xx}	349.687
α_{xy}	16.8106
α_{yy}	263.897
α_{xz}	11.930
α_{yz}	-5.925
α_{zz}	136.058
α_{tot} (x10^{-24})	37.10
Dipole moment	
μ_x	-5.192
μ_y	6.645
μ_z	-0.556
μ	8.451
Frontier molecular orbital	
E_{HOMO}	-6.3538
E_{LUMO}	-2.1418
$E_{HOMO} - E_{LUMO}$	4.2120

Table 6 First-order molecular hyperpolarizability (β) values some hydrazide.

Compound	β(x10^{-30}) esu	Ref
4-benzoylpyridine isonicotinyl hydrazone monohydrate	2.799 (~10 times of urea)	[15]
Benzophenone-2-furoyl hydrazone	0.817 (~2.5 times of urea)	[16]
(E)-N'-(diphenylmethylene)isonicotinohydrazide dihydrate	1.673 (~ 5 times of urea)	[17]
(E)-N′-((Pyridin-2-yl)methylene)benzohydrazide monohydrate	4.360 (12 times of urea)	[23]
N′-(2-methyl-3-phenylallylidene)nicotinohydrazide	18.380	[24]
(E)-N'-((4-fluorophenyl)(phenyl)methylene)isonicotinohydrazide dihydrate	23.458 (~84 times of urea)	Present work

Table 7. Second order perturbation theory analysis of Fock matrix in NBO basis for FPMI

Donor (i)	[a]ED(i)/(e)		Acceptor (j)	[a]ED(j)/(e)	[b]E(2)/kJ mol	[c]E(j)-E(i) /a.u	[d]F(i,j)/a.u
(σ) C 10 - C 11	1.96577	RY*	(σ) C 2	0.0048	1.3	1.94	0.045
		BD*	(σ) C 12 - C 13	0.02417	1	1.2	0.031
		BD*	(π) C 12 - C 13	0.3722	0.9	0.66	0.024
		BD*	(σ) N 22 - N 23	0.02204	5.25	1.03	0.066
(σ) C 10 - C 12	1.97447	RY*	(σ) C 11	0.0065	2.1	1.84	0.056
		BD*	(σ) C 10 - N 22	0.01772	1.44	1.25	0.038
		BD*	(σ) C 13 - C 15	0.01408	2.35	1.22	0.048
(σ) C 10 - N 22	1.98537	RY*	(σ) C 11	0.0065	0.97	2.08	0.04
		BD*	(σ) C 12 - C 14	0.02418	0.65	1.44	0.027
		BD*	(σ) N 23 - C 25	0.07764	2.33	1.34	0.051
(σ) C 19 - F 44	1.99588	RY*	(σ) C 19	0.00924	0.85	1.84	0.035
		BD*	(σ) C 13 - C 15	0.01408	1.33	1.59	0.041
		BD*	(σ) C 14 - C 17	0.014	1.32	1.59	0.041
(σ) N 22 - N 23	1.98544	RY*	(π) C 10	0.00514	1.04	1.8	0.039
		BD*	(σ) C 10 - C 11	0.03727	3.28	1.33	0.059
		BD*	(σ) C 10 - N 22	0.01772	0.57	1.45	0.026
(σ) N 23 - H 24	1.9876	RY*	(σ) N 22	0.00669	0.97	1.61	0.035
		BD*	(σ) C 25 - O 26	0.01949	3.67	1.27	0.061
		BD*	(π) C 25 - O 26	0.29574	0.54	0.72	0.019
(σ) N 23 - C 25	1.98887	RY*	(σ) N 22	0.00669	1.44	1.75	0.045
		BD*	(σ) C 10 - N 22	0.01772	2.11	1.42	0.049
		BD*	(σ) N 22 - N 23	0.02204	0.69	1.21	0.026
		BD*	(σ) N 23 - H 24	0.04055	0.59	1.26	0.025
		BD*	(σ) C 25 - O 26	0.01949	0.76	1.41	0.029
		BD*	(σ) C 27 - C 29	0.0209	1.28	1.4	0.038
(σ) C 25 - O 26	1.99438	RY*	(σ) C 25	0.01648	1.31	1.86	0.044
		BD*	(σ) N 23 - C 25	0.07764	0.75	1.48	0.03
(σ) C 30 - N 34	1.98754	RY*	(π) C 28	0.00211	1.19	1.59	0.039
		BD*	(σ) C 30 - H 35	0.01943	0.54	1.3	0.024
		BD*	(σ) C 32 - N 34	0.01615	1.18	1.36	0.036
		BD*	(σ) C 32 - H 36	0.02165	1.95	1.33	0.046
(σ) C 32 - N 34	1.98689	RY*	(π) C 29	0.00257	1.44	1.65	0.044
		BD*	(σ) C 30 - N 34	0.01686	1.2	1.36	0.036
		BD*	(σ) C 30 - H 35	0.01943	2.39	1.29	0.05
(σ) N 22	-1.99928	BD*	(σ) C 10 - C 11	0.03727	0.52	14.66	0.079
		BD*	(σ) C 10 - C 12	0.04447	0.96	14.63	0.107
		BD*	(σ) N 23 - H 24	0.04055	0.64	14.62	0.087
		BD*	(σ) N 23 - C 25	0.07764	0.64	14.64	0.088
(σ) O 26	-1.99975	RY*	(σ) C 25	0.01648	5.7	19.7	0.3
		BD*	(σ) N 23 - C 25	0.07764	0.59	19.32	0.097
(σ) F 44	-1.99994	RY*	(σ) C 19	0.00924	2.53	25.27	0.226
(σ) N 23	1.64853	BD*	(π) C 10 - N 22	0.20304	27.84	0.29	0.084
		BD*	(σ) C 25 - O 26	0.01949	1.12	0.85	0.03
		BD*	(π) C 25 - O 26	0.29574	51.58	0.3	0.113
(π) O 26	1.85975	BD*	(σ) N 23 - C 25	0.07764	28.12	0.7	0.127
		BD*	(σ) C 25 - C 27	0.06747	17.44	0.67	0.098
(π) C 32 - N 34	0.37342	BD*	(π) C 27 - C 29	0.32643	155.83	0.02	0.088
		BD*	(π) C 28 - C 30	0.30186	205.07	0.01	0.079
(π) C 10 - N 22	0.20304	BD*	(π) C 3 - C 11	0.37837	75.23	0.02	0.066
(π) C 32 - N 34	1.70795	BD*	(π) C 27 - C 29	0.32643	13.78	0.33	0.06
		BD*	(π) C 28 - C 30	0.30186	26.96	0.32	0.083
(π) C 28 - C 30	1.64346	BD*	(π) C 27 - C 29	0.32643	21.06	0.29	0.071
		BD*	(π) C 32 - N 34	0.37342	16.58	0.27	0.06

[a]ED is the occupation number.
[b]$E^{(2)}$is the energy of hyperconjugative interactions.
[c]Energy difference between donor and acceptor *i* and *j* NBO orbitals.
[d]*F(i, j)* is the Fock matrix element between *i* and *j* NBO orbitals.

Figure captions

Fig 1. Photo images of as–grown FPMI crystals.

Fig 2. UV-vis spectra of (a) Experimental (b) ZINDO (c) TD-DFT(d) CIS.

Fig 3. Simulated and experimental indexed powder XRD patterns of FPMI.

Fig 4. (a) *ORTEP* (b) Optimized molecular structure and (c) Packing diagram of FPMI.

Fig 5. Molecular surface images of FPMI.

Fig 6.(a) Mulliken atomic charge distribution and (b) Mulliken plot of FPMI.

Fig 7. Hirshfeld surface analysis of FPMI (a) *dnorm* (Front view) (b) *dnorm (*back view) (c) *de* (d) *di* (e) *curvedness* (f) *shapeindex.*

Fig 8. Crystal packing showing hydrogen bonding interactions along 'a' axis.

Fig 9. Crystal packing showing hydrogen bonding interactions along 'b' axis.

Fig 10 . Crystal packing showing hydrogen bonding interactions along 'c' axis.

Fig 11. Deformation density surface of FPMI.

Fig 12. Fingerprint plots of FPMI.

Fig 13. Relative contribution of various intermolecular interactions in FPMI.

Fig.1

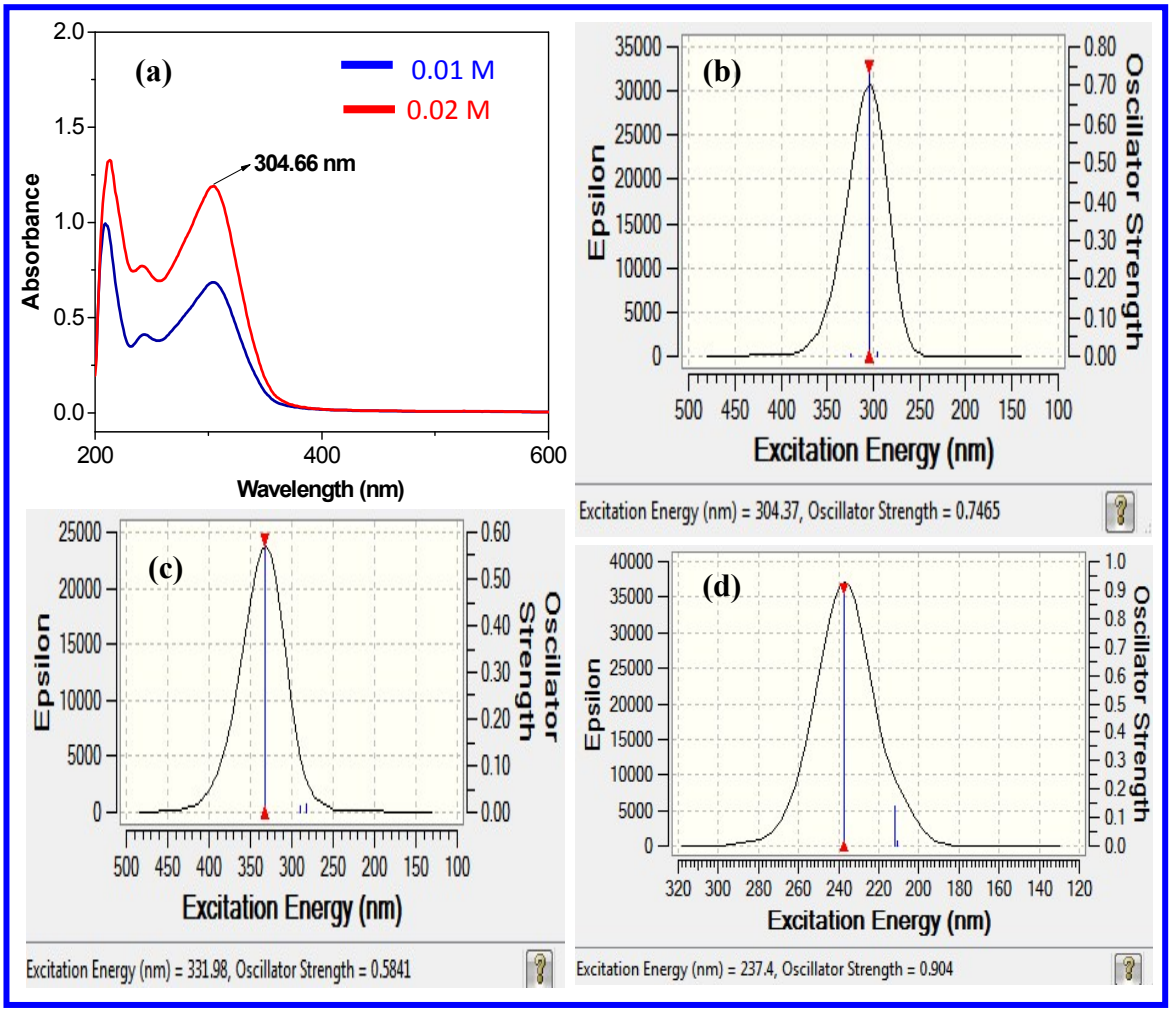

Fig. 2

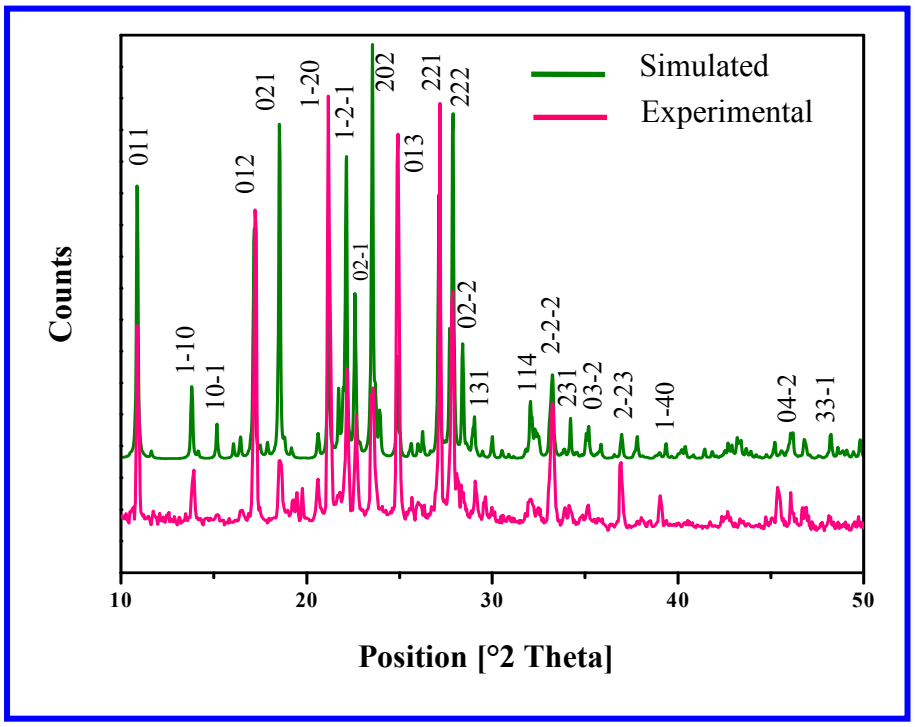

Fig. 3

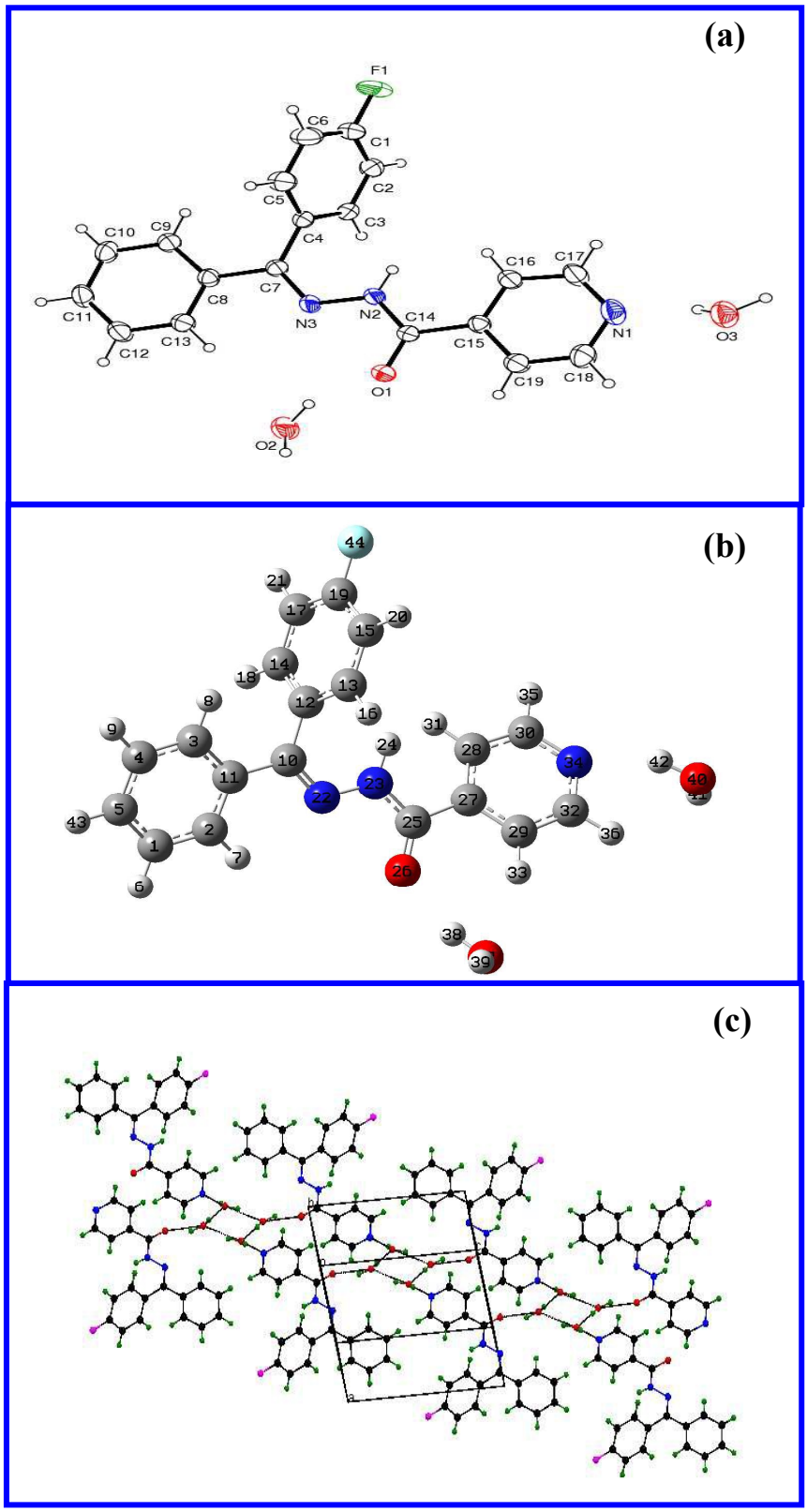

Fig. 4

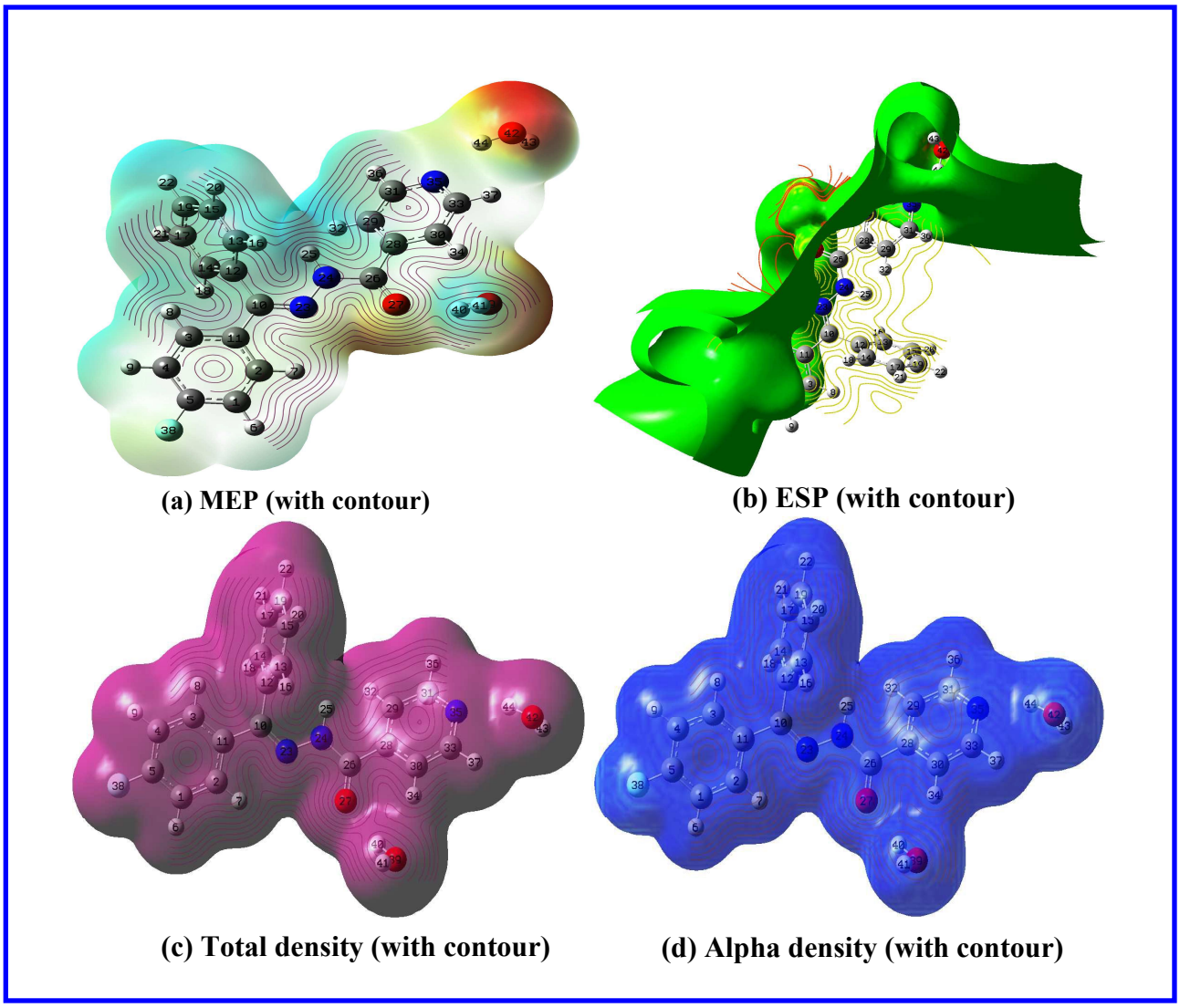

Fig. 5

a

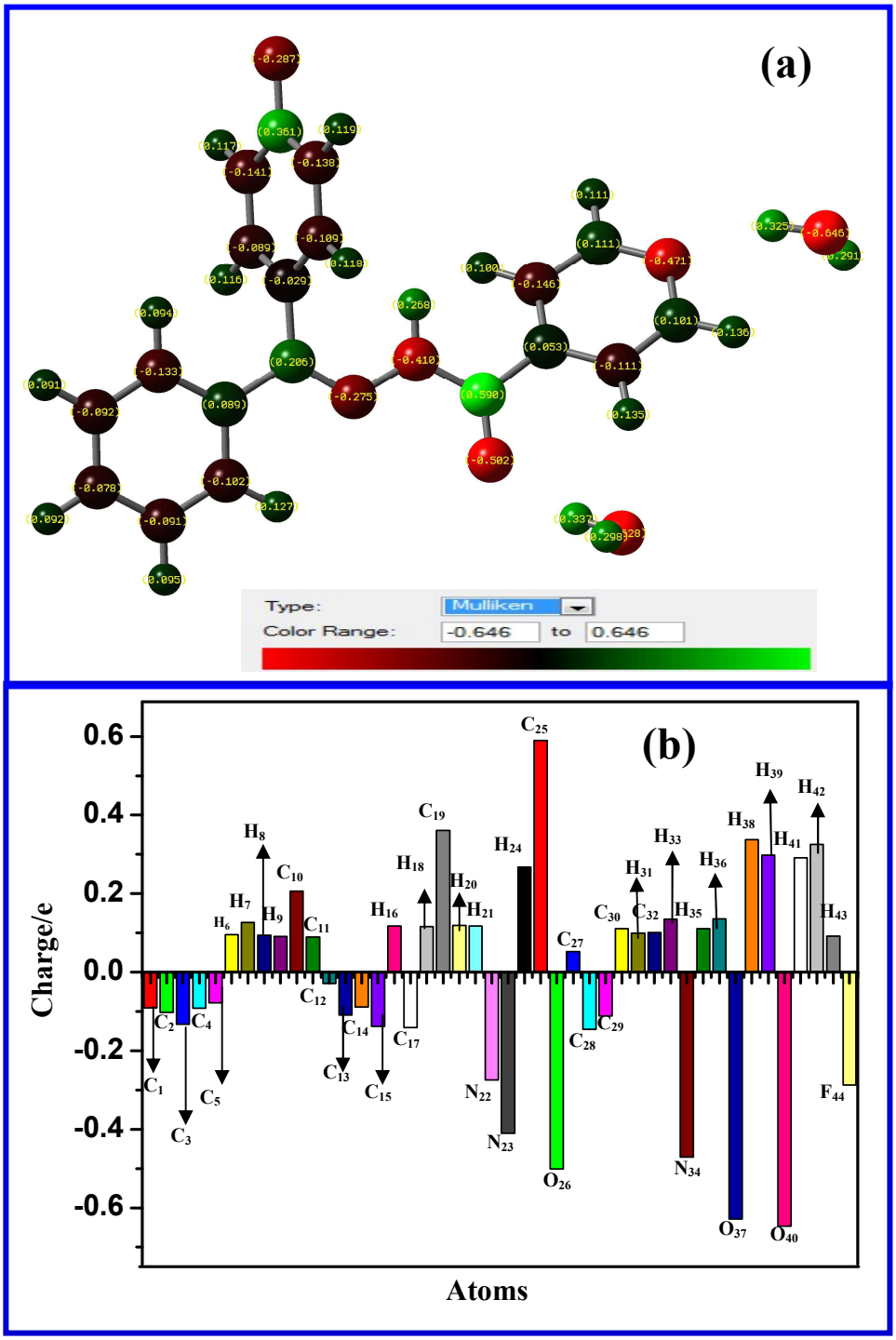

Fig. 6

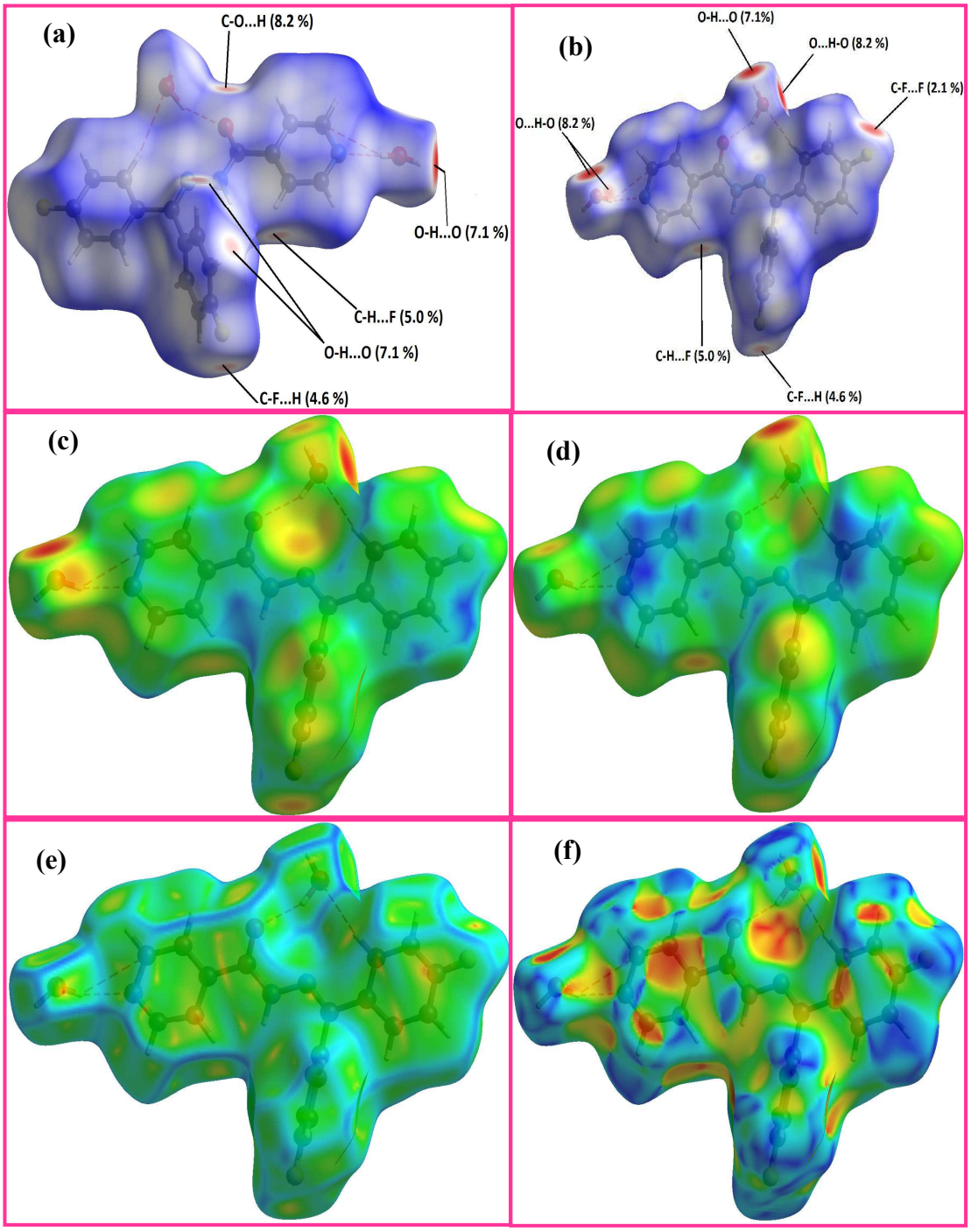

Fig. 7

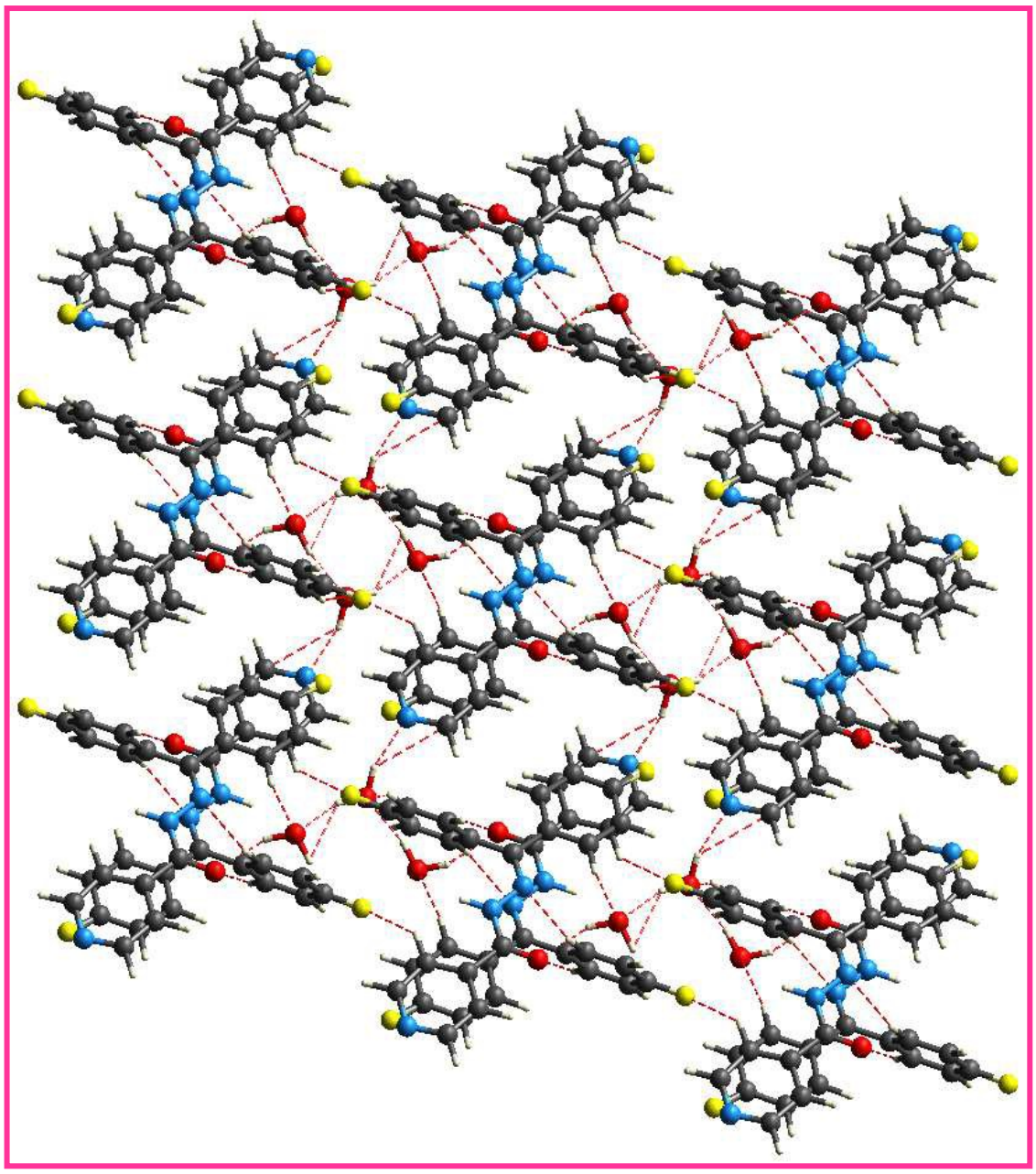

Fig. 8

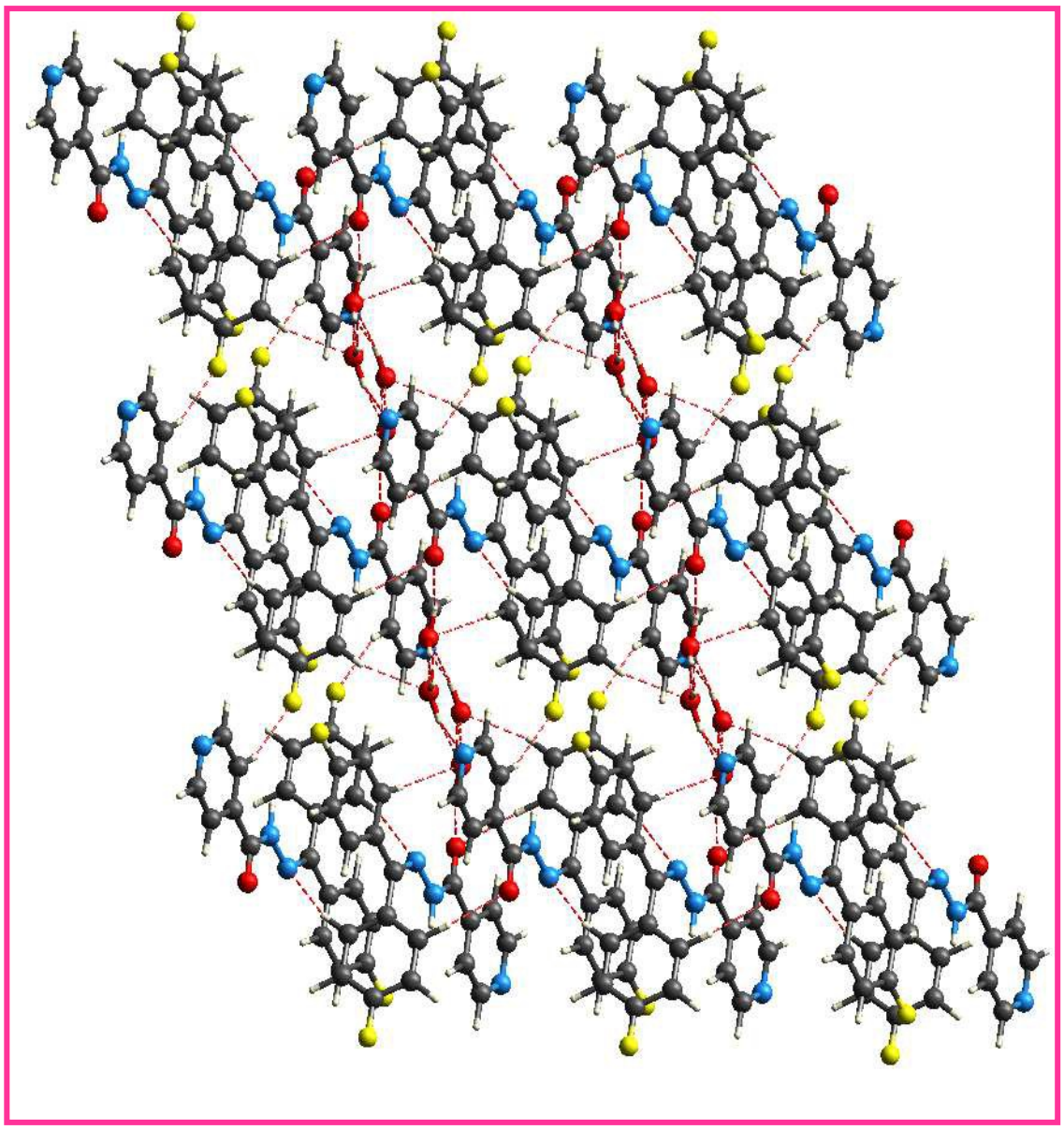

Fig. 9

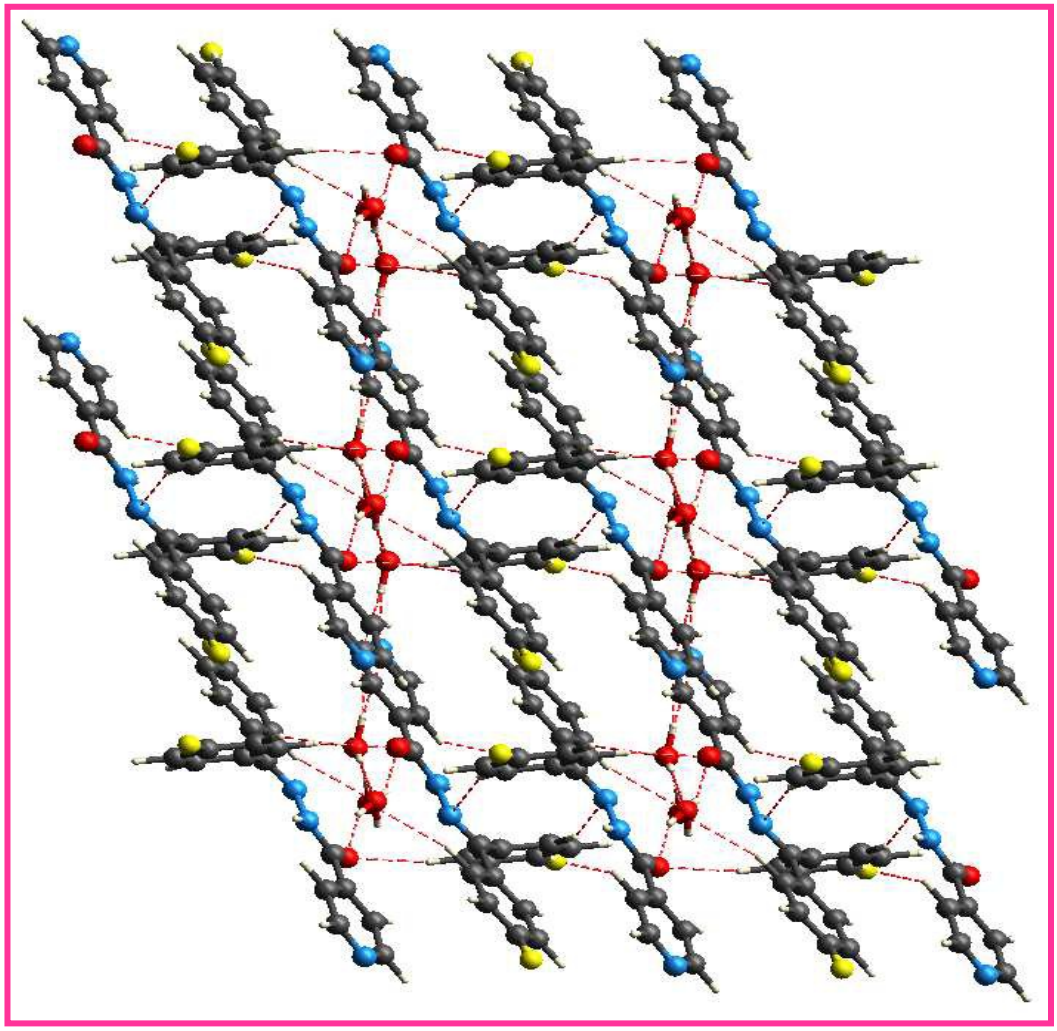

Fig. 10

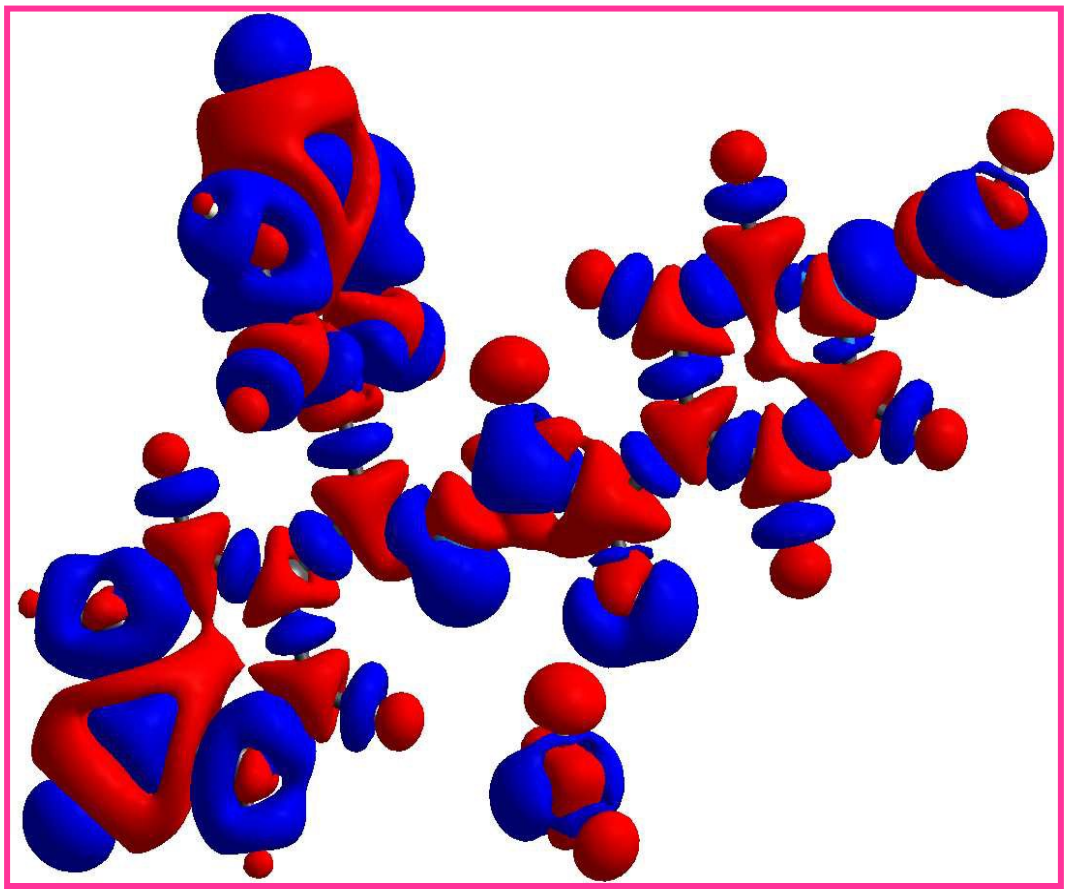

Fig. 11

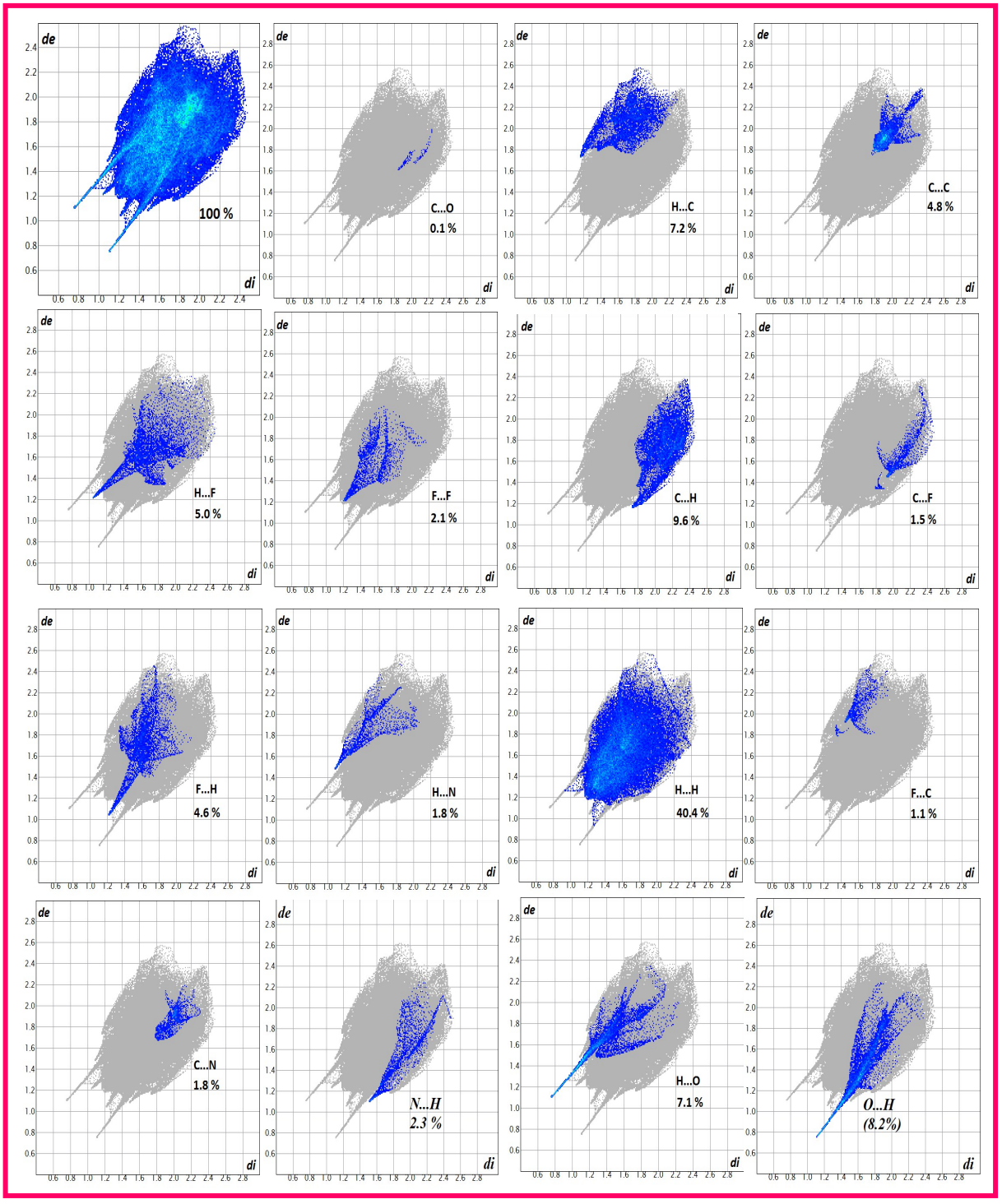

Fig. 12

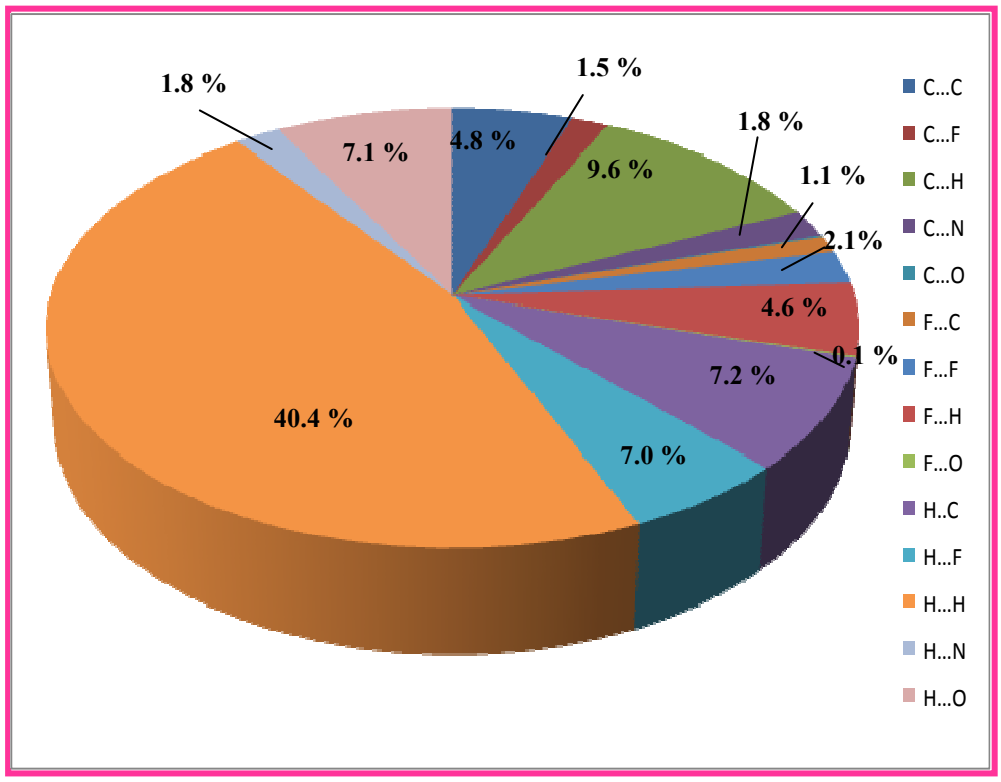

Fig. 13